arXiv:1409.1167v1 [math.NA] 3 Sep 2014

Globally convergent and adaptive finite element methods in imaging of buried objects from experimental backscattering radar measurements

Larisa Beilina[1]*, Nguyen Trung Thành[2], Michael V. Klibanov[3]
and John Bondestam Malmberg[1]
[1]Department of Mathematical Sciences,
Chalmers University of Technology and Gothenburg University,
SE-42196 Gothenburg, Sweden
Emails: larisa@chalmers.se, john.bondestam.malmberg@chalmers.se.
[2]Department of Mathematics, Iowa State University,
Ames, IA 50011, USA. Email: thanh@iastate.edu.
[3]Department of Mathematics & Statistics, University of North Carolina at Charlotte,
Charlotte, NC 28223, USA. Email: mklibanv@uncc.edu.

Abstract

We consider a two-stage numerical procedure for imaging of objects buried in dry sand using time-dependent backscattering experimental radar measurements. These measurements are generated by a single point source of electric pulses and are collected using a microwave scattering facility which was built at the University of North Carolina at Charlotte. Our imaging problem is formulated as the inverse problem of the reconstruction of the spatially distributed dielectric permittivity $\varepsilon_r(\mathbf{x})$, $\mathbf{x} \in \mathbb{R}^3$, which is an unknown coefficient in Maxwell's equations.

On the first stage an approximately globally convergent method is applied to get a good first approximation for the exact solution. On the second stage a local adaptive finite element method is applied to refine the solution obtained on the first stage. The two-stage numerical procedure results in accurate imaging of all three components of interest of targets: shapes, locations and refractive indices. In this paper we briefly describe methods and present new reconstruction results for both stages.

Keywords: Inverse scattering, refractive indices, approximately globally convergent algorithm, adaptive finite element method.

AMS classification codes: 65N15, 65N30, 35J25.

1 Introduction

In this paper we consider the problem of reconstruction of refractive indices, shapes and locations of buried objects in the dry sand from backscattering time-dependent experimental data using the two-stage numerical procedure presented in [6, 12, 14, 26]. Our problem is a coefficient inverse problem (CIP) for Maxwell's equations in three dimensions. Experimental data were collected using a microwave scattering facility which was built at the University of North Carolina at Charlotte, USA. Our experimental data are collected using a single location of the source. The backscattered signal is measured on a part of a plane. Our potential applications are in the imaging of explosives, such as land mines and improvised

*Corresponding author

explosive devices. This work is a continuation of our recent works on this topic, where we have treated a much simpler case of experimental data for targets placed in air [13, 14, 21].

The two-stage numerical procedure means that we combine two different methods to solve our CIP. On the first stage the approximately globally convergent method of [12] is applied in order to obtain a good first approximation for the exact solution. We have presented results of reconstruction on this stage in our publications [13, 21] for objects placed in air. In our recent study [22] we presented reconstructions of twenty-five objects which show that the method of [12] works well in estimating the dielectric constants (equivalently, refractive indices) and locations of buried objects.

In [3] it was investigated why a minimizer of the Tikhonov functional is indeed closer to the exact solution than the first guess of this minimizer. Because of that it makes sense improve the solution which we have obtained on the first stage of our two-stage numerical procedure. To do that the local adaptive finite element method of [10] is applied by taking the solution of the first stage as the starting point in the minimization of a Tikhonov functional in order to obtain better approximations and shapes of objects on the adaptively refined meshes. In [14] it was shown that using the adaptive finite element method all three components of interest for targets placed in the air can be simultaneously imaged: refractive indices, shapes and locations.

Compared to imaging of targets placed in the air (see [13, 14, 21]), there are three main difficulties in imaging of buried targets: (i) the signals of targets are much weaker than those when the targets are in air, (ii) these signals may overlap with the reflection from the ground's surface, which makes them difficult to distinguish, and (iii) the reflection from the grounds surface may dominate the target's signals after the Laplace transform since the kernel of the Laplace transform decays exponentially with respect to time. We have handled this difficulty in [22] via a new data preprocessing procedure. This procedure results in preprocessed data, which are used as the input for our globally convergent algorithm, that is, the input for the first stage of our method.

It is notable that we have experimentally observed a rare superresolution phenomenon and have numerically reconstructed the corresponding image (see section 7). The resolution limit which follows from the Born approximation, that is, in the diffraction limit, is $\lambda/2$, where λ is the wavelength of the signal. However, we have resolved two targets with the distance $\lambda/4.5$ between their surfaces. It was shown in, for instance [24], that the superresolution can occur because of nonlinear scattering, and our algorithm is nonlinear, including the step of extraction of the target's signal in our data preprocessing procedure [22]. Experimentally the superresolution phenomenon was demonstrated in [17]. We also refer to the recent work [1] where the superresolution is discussed.

An outline of this paper follows. In section 2 we briefly describe the approximate globally convergent method. In section 3 we present the forward, inverse, and adjoint problems as well as the Tikhonov functional for the second stage. In section 4 we describe the finite element method used in computations and in section 5 we investigate general framework for a posteriori error estimation for CIPs. In section 6 we describe the mesh refinement recommendation and the adaptive algorithm. In section 7 we present results of our computations.

2 The first stage

In this section we state the forward and inverse problems which we consider on the first stage. We also briefly outline the globally convergent method of [12] and present the algorithm used in computations of the first stage.

2.1 Forward and inverse problems

Let $\Omega \subset \mathbb{R}^3$ be a convex bounded domain with the boundary $\partial\Omega \in C^3$. Denote the spatial coordinates by $\mathbf{x} = (x, y, z) \in \mathbb{R}^3$. Let $C^{k+\alpha}$ be Hölder spaces, where $k \geq 0$ is an integer and $\alpha \in (0, 1)$. We consider the propagation of the electromagnetic wave in $\mathbb{R}^3$ generated by an incident plane wave. On the first

stage we model the wave propagation by the following Cauchy problem for the scalar wave equation

$$\varepsilon_{\mathrm{r}}(\mathbf{x})\frac{\partial^2 u}{\partial t^2}(\mathbf{x},\, t) - \Delta u(\mathbf{x},\, t) = \delta(z - z_0)f(t), \qquad (\mathbf{x},\, t) \in \mathbb{R}^3 \times (0,\, \infty), \tag{1}$$

$$u(\mathbf{x},\, 0) = 0, \quad \frac{\partial u}{\partial t}(\mathbf{x},\, 0) = 0, \qquad \mathbf{x} \in \mathbb{R}^3. \tag{2}$$

Here $f\,(t) \not\equiv 0$ is the time-dependent incident plane wave at the plane $\{z = z_0\}$, u is the total wave generated by $f(t)$ and propagating along the z-axis.

Let the function $E\,(\mathbf{x},\, t)$ represent the voltage of one component E_2 of the electric field $E\,(\mathbf{x},\, t) = (E_1,\, E_2,\, E_3)\,(\mathbf{x},\, t)$. In our experiments the component E_2 corresponds to the electromagnetic wave which is sent into the medium. Our mathematical model of the first stage uses only the single equation (1) with $u = E_2$ instead of the full Maxwell's system. We can do such approximation since it was shown numerically in [9] that the component E_2 of the electric field E dominates the other two components in the case we consider. See also [12] where a similar scalar wave equation was used to work with transmitted experimental data.

The function ε_{r} in (1) represents the spatially distributed dielectric permittivity. We assume that ε_{r} is unknown inside the domain $\Omega \subset \mathbb{R}^3$ and is such that

$$\varepsilon_{\mathrm{r}} \in C^{\alpha}\left(\mathbb{R}^3\right), \quad \varepsilon_{\mathrm{r}}(\mathbf{x}) \in [1,\, b] \text{ for } \mathbf{x} \in \mathbb{R}^3, \quad \varepsilon_{\mathrm{r}}(\mathbf{x}) = 1 \text{ for } \mathbf{x} \in \mathbb{R}^3 \setminus \Omega, \tag{3}$$

where $b > 1$ is a constant. We assume that the set of admissible coefficients in (3) is known. Let $\Gamma \subset \partial\Omega$ be a part of the boundary $\partial\Omega$. In our experiments the plane wave is initialized outside of the domain $\overline{\Omega}$, that is $\overline{\Omega} \cap \{z = z_0\} = \varnothing$.

Coefficient Inverse Problem (CIP). *Determine the function $\varepsilon_{\mathrm{r}}\,(\mathbf{x})$ for $\mathbf{x} \in \Omega$, assuming that the following function g is known for a single incident plane wave generated at the plane $\{z = z_0\}$ outside of $\overline{\Omega}$:*

$$u\,(\mathbf{x},\, t) = g\,(\mathbf{x},\, t) \;\; \forall\,(\mathbf{x},\, t) \in \Gamma \times (0,\, \infty)\,.$$

Global uniqueness theorems for multidimensional CIPs with a single measurement are currently known only under the assumption that at least one of initial conditions does not equal zero in the entire domain $\overline{\Omega}$ [12, 16]. However, this is not our case and the method of Carleman estimates is inapplicable to our CIP. Thus, we simply assume that uniqueness of our CIP holds.

2.2 The globally convergent method

Here we briefly present approximately globally convergent method of [12].

We perform a Laplace transformation

$$\tilde{u}(\mathbf{x},\, s) = \int\limits_0^{\infty} u(\mathbf{x},\, t)e^{-st}\,\mathrm{d}t,$$

where s is a positive parameter which we call *pseudo frequency*. We assume that $s \geq \underline{s} > 0$ and denote by $\tilde{f}(s)$ the Laplace transform of $f(t)$. We assume that $\tilde{f}(s) \neq 0$ for all $s \geq \underline{s}$. Define $w(\mathbf{x},\, s) := \tilde{u}(\mathbf{x},\, s)/\tilde{f}(s)$. The function w satisfies the equation

$$\Delta w(\mathbf{x},\, s) - s^2\varepsilon_{\mathrm{r}}(\mathbf{x})w(\mathbf{x},\, s) = -\delta(z - z_0), \quad \mathbf{x} \in \mathbb{R}^3, \;\; s \geq \underline{s}. \tag{4}$$

It was shown in [22] that $w(\mathbf{x},\, s) > 0$ and $\lim_{|\mathbf{x}|\to\infty}\left[w\,(\mathbf{x},\, s) - w_0(\mathbf{x},\, s)\right] = 0$, where $w_0\,(\mathbf{x},\, s) := e^{-s|z-z_0|}/\,(2s)$ is a solution of equation (4) for the case $\varepsilon_{\mathrm{r}}\,(\mathbf{x}) \equiv 1$, which decays to zero as $|z| \to \infty$. Next, introduce the function v by $v(\mathbf{x},\, s) := \ln\big(w(\mathbf{x},\, s)\big)/s^2$ and substitute $w = \exp(vs^2)$ into (4). By noting that $\overline{\Omega} \cap \{z = z_0\} = \varnothing$, we obtain the following equation for the explicit computation of the coefficient ε_{r}:

$$\Delta v(\mathbf{x},\, s) + s^2|\nabla v(\mathbf{x},\, s)|^2 = \varepsilon_{\mathrm{r}}(\mathbf{x}), \quad \mathbf{x} \in \Omega, \;\; s \geq \underline{s}. \tag{5}$$

Next, we eliminate the unknown coefficient $\varepsilon_{\mathrm{r}}(\mathbf{x})$ from (5) by taking the derivative with respect to s both sides of (5). Denote by $q := \frac{\partial v}{\partial s}$, then

$$v(\mathbf{x},\, s) = -\int_s^{\infty} q(\mathbf{x},\, \tau)\,\mathrm{d}\tau = -\int_s^{\bar{s}} q(\mathbf{x},\, \tau)\,\mathrm{d}\tau + V(\mathbf{x}),$$

where $\bar{s} > \underline{s}$. We call the function $V(\mathbf{x}) = v(\mathbf{x},\, \bar{s})$ the "tail function"and define it by

$$V(\mathbf{x}) = \frac{\ln w(\mathbf{x},\, \bar{s})}{\bar{s}^2}. \tag{6}$$

From (5) we obtain the following equation for two unknown functions q and V

$$\begin{aligned} &\Delta q(\mathbf{x},\, s) - 2s^2 \nabla q(\mathbf{x},\, s) \cdot \int_s^{\bar{s}} \nabla q(\mathbf{x},\, \tau)\,\mathrm{d}\tau + 2s^2 \nabla V(\mathbf{x}) \cdot \nabla q(\mathbf{x},\, s) \\ &\qquad + 2s \left| \int_s^{\bar{s}} \nabla q(\mathbf{x},\, \tau)\,\mathrm{d}\tau \right|^2 - 4s \nabla V(\mathbf{x}) \cdot \int_s^{\bar{s}} \nabla q(\mathbf{x},\, \tau)\,\mathrm{d}\tau + 2s\,|\nabla V(\mathbf{x})|^2 = 0, \end{aligned} \tag{7}$$

for $\mathbf{x} \in \Omega$ and $s \in (\underline{s},\, \bar{s})$.

To find the tail function V we use an iterative procedure presented in the next section, see [13, 21] for details of this procedure. The function q satisfies the following boundary condition

$$q(\mathbf{x},\, s) = \psi(\mathbf{x},\, s), \quad \mathbf{x} \in \partial\Omega, \tag{8}$$

where $\psi(\mathbf{x},\, s) = \frac{\partial}{\partial s}\left[\frac{\ln \varphi(\mathbf{x},\, s)}{s^2}\right]$ with $\varphi(\mathbf{x},\, s) = \int_0^{\infty} g(\mathbf{x},\, t) e^{-st}\,\mathrm{d}t / \tilde{f}(s)$.

2.3 Iterative procedure and description of the approximate globally convergent algorithm

In our iterative procedure we divide the pseudo frequency interval $[\underline{s},\, \bar{s}]$ into N sub-intervals $\bar{s} = s_0 > s_1 > \cdots > s_N = \underline{s}$ of the step size h such that $s_n - s_{n+1} = h$. We approximate the function q by a piecewise constant function with respect s, $q(\mathbf{x},\, s) \approx q_n(\mathbf{x})$, $s \in (s_n,\, s_{n-1}]$, $n = 1,\, \ldots,\, N$, and set $q_0 \equiv 0$. Next, we multiply equation (7) by the Carleman Weight Function $\exp\left[\Lambda\,(s - s_{n-1})\right]$, $s \in (s_n,\, s_{n-1})$, where $\Lambda \gg 1$ is a large parameter chosen in the computations, and integrate with respect to s over every pseudo frequency interval $[s_n,\, s_{n-1}]$. Finally, we get a system of elliptic equations for the functions q_n for $\mathbf{x} \in \Omega$:

$$\begin{aligned} &\Delta q_n(\mathbf{x}) + A_{1,\,n} \nabla q_n(\mathbf{x}) \cdot \left(\nabla V_n(\mathbf{x}) - \nabla \overline{q_{n-1}}(\mathbf{x})\right) \\ &\qquad = A_{2,n} |\nabla q_n(\mathbf{x})|^2 + A_{3,\,n} |\nabla V_n(\mathbf{x}) - \nabla \overline{q_{n-1}}(\mathbf{x})|^2, \end{aligned} \tag{9}$$

where $A_{i,\,n}$, $i = 1,\, 2,\, 3$, are some coefficients defined in [12] and can be computed analytically and $\overline{q_{n-1}} = h \sum_{j=0}^{n-1} q_j$. The tail function $V = V_n$ is approximated iteratively, see algorithm below. The discretized version of the boundary condition (8) is given by

$$q_n(\mathbf{x}) = \psi_n(\mathbf{x}) := \frac{1}{h} \int_{s_n}^{s_{n-1}} \psi(\mathbf{x},\, s)\,\mathrm{d}s \approx \frac{1}{2}[\psi(\mathbf{x},\, s_n) + \psi(\mathbf{x},\, s_{n-1})], \quad \mathbf{x} \in \partial\Omega. \tag{10}$$

We also note that the first term on the right hand side of (9) is negligible compared to the other terms since $|A_{2,\,n}| \sim \Lambda^{-1}$ for sufficiently large Λ, while $|A_{i,\,n}| \sim \Lambda^0$, $i = 1,\, 3$. Thus, we set $A_{2,\,n} |\nabla q_n|^2 = 0$. The system of elliptic equations (9) with boundary conditions (10) is solved sequentially starting from $n = 1$. To solve it we use following algorithm:

Globally convergent algorithm

- Compute the first tail function V_0 (see [13] for details). Set $q_0 \equiv 0$.
- For $n = 1, 2, \ldots, N$
  1. Set $q_{n,0} = q_{n-1}$, $V_{n,1} = V_{n-1}$
  2. For $i = 1, 2, \ldots, m_n$
     - Find $q_{n,i}$ by solving (9)–(10) with $V_n := V_{n,i}$.
     - Compute $v_{n,i} = -hq_{n,i} - \overline{q_{n-1}} + V_{n,i}$.
     - Compute $\varepsilon_{r,n,i}$ via (5). Then solve the forward problem (1)–(2) with the new computed coefficient $\varepsilon_r := \varepsilon_{r,n,i}$, compute $w := w_{n,i}$ and update the tail $V_{n,i+1}$ by (6).
  3. Set $q_n = q_{n,m_n}$, $\varepsilon_{r,n} = \varepsilon_{r,n,m_n}$, $V_n = V_{n,m_n+1}$ and go to the next frequency interval $[s_{n+1}, s_n]$ if $n < N$. If $n = N$, then stop.

Stopping criteria of this algorithm with respect to i and n are derived computationally and is presented in [13, 21]. We denote the solution obtained at this stage by $\varepsilon_{r,glob}$.

3 Statement of Forward and Inverse Problems on the second stage

On the second stage we model the electromagnetic wave propagation in an isotropic and non-magnetic space with permeability $\mu = 1$ in $\mathbb{R}^3$ with the dimensionless coefficient ε_r, which describes the spatially distributed dielectric permittivity of the medium. We consider the following Cauchy problem in the model problem for the electric field $E(\mathbf{x}, t) = (E_1, E_2, E_3)(\mathbf{x}, t)$

$$\begin{aligned}
&\varepsilon_r(\mathbf{x})\frac{\partial^2 E}{\partial t^2}(\mathbf{x}, t) + \nabla \times \big(\nabla \times E(\mathbf{x}, t)\big) = (0, \delta(z - z_0)f(t), 0), && (\mathbf{x}, t) \in \mathbb{R}^3 \times (0, T),\\
&\nabla \cdot \big(\varepsilon_r(\mathbf{x})E(\mathbf{x}, t)\big) = 0, && (\mathbf{x}, t) \in \mathbb{R}^3 \times (0, T),\\
&E(\mathbf{x}, 0) = 0, \quad \frac{\partial E}{\partial t}(\mathbf{x}, 0) = 0, && \mathbf{x} \in \mathbb{R}^3.
\end{aligned} \tag{11}$$

In the above equation $f(t) \not\equiv 0$ is the time-dependent waveform of the incident plane wave. This wave propagates along the z-axis and is incident at the plane $\{z = z_0\}$.

We assume that the coefficient ε_r of equation (11) is the same as in (3). Let again $\Gamma \subset \partial\Omega$ be a part of the boundary $\partial\Omega$.

Coefficient Inverse Problem (CIP). *Suppose that the coefficient ε_r satisfies* (11). *Determine the function $\varepsilon_r(\mathbf{x})$, $\mathbf{x} \in \Omega$, assuming that the following function g is known for a single incident plane wave:*

$$E(\mathbf{x}, t) = g(\mathbf{x}, t) \ \forall (\mathbf{x}, t) \in \Gamma \times (0, T). \tag{12}$$

In (12) the function g models time dependent measurements of the electromagnetic field at the part Γ of the boundary $\partial\Omega$ of the domain Ω in which coefficient ε_r is unknown. The uniqueness of the above CIP in the multidimensional case is currently known only if we will consider in (11) a Gaussian function $\delta_\theta(z - z_0)$ centered around z_0, which approximates the function $\delta(z - z_0)$, or if at least one of initial conditions in (11) is not zero. We again assume that uniqueness holds for our CIP.

The function E in (11) represents the voltage of one component of the electric field $E(\mathbf{x}, t) = (E_1, E_2, E_3)(\mathbf{x}, t)$. In our computer simulations of section 7.5 the incident field has only one non-zero component E_2. This component propagates along the z-axis until it reaches the target, where it is scattered. When solving the forward problem in our computations of section 7.5, we first generate the data (12) by solving the problem (11) for the case when the function ε_r is taken as the one reconstructed by the globally convergent method. Next, the computed component E_2 on the surface Γ is replaced with the measured data. The other two components, E_1 and E_3, are left the same as the ones obtained by the solution of the problem (11), see details in [14].

3.1 Domain decomposition finite element/finite difference method

To solve the problem (11) numerically we choose a bounded domain G such that $\Omega \subset G$. In our computations of the second stage we use the domain decomposition finite element/finite difference method of [9]. To do that we decompose G as $G = \Omega_{\rm FEM} \cup \Omega_{\rm FDM}$ with $\Omega_{\rm FEM} = \Omega$. Then, in computations, in $\Omega_{\rm FEM}$ a finite element method is used while in $\Omega_{\rm FDM}$ a finite difference method is used, see details in [9].

Using (3) we have that

$$\varepsilon_{\rm r}(\mathbf{x}) \geq 1, \text{ for } \mathbf{x} \in \Omega_{\rm FEM},$$
$$\varepsilon_{\rm r}(\mathbf{x}) = 1, \text{ for } \mathbf{x} \in \Omega_{\rm FDM}.$$

As in [9] in our computations we used the following stabilized model problem with the parameter $\xi \geq 1$:

$$\varepsilon_{\rm r}(\mathbf{x})\frac{\partial^2 E}{\partial t^2}(\mathbf{x},\, t) + \nabla \times \big(\nabla \times E(\mathbf{x},\, t)\big) - \xi \nabla\Big(\nabla \cdot \big(\varepsilon_{\rm r}(\mathbf{x}) E(\mathbf{x},\, t)\big)\Big) = 0, \qquad (\mathbf{x},\, t) \in G \times (0,\, T), \tag{13}$$

$$E(\mathbf{x},\, 0) = 0, \quad \frac{\partial E}{\partial t}(\mathbf{x},\, 0) = 0, \qquad \mathbf{x} \in G. \tag{14}$$

To determine boundary conditions for (13), (14), we choose the domains Ω and G such that

$$\Omega = \Omega_{\rm FEM} = \{\mathbf{x} = (x,\, y,\, z) : -a < x < a,\, -b < y < b,\, -c < z < c'\},$$

$$G = \{\mathbf{x} = (x,\, y,\, z) : -A < x < A,\, -B < y < B,\, -C < z < z_0\},$$

where $0 < a < A$, $0 < b < B$, $-C < -c < c' < z_0$, and $\Omega_{\rm FDM} = G \setminus \Omega_{\rm FEM}$. Denote by

$$\partial_1 G := \overline{G} \cap \{z = z_0\}, \quad \partial_2 G := \overline{G} \cap \{z = -C\}, \quad \partial_3 G := \partial G \setminus (\partial_1 G \cup \partial_2 G).$$

The backscattering side of Ω is $\Gamma = \partial\Omega \cap \{z = c'\}$. Next, define $\partial_i G_T := \partial_i G \times (0,\, T)$, $i = 1,\, 2,\, 3$. Let $t' \in (0,\, T)$ be a number, and we assume that the function $f(t) \in C[0,\, t']$ and $f(t) = 0$ for $t > t'$.

Then boundary conditions for (13)–(14) are:

$$E(\mathbf{x},\, t) = (0,\, f(t),\, 0), \qquad (\mathbf{x},\, t) \in \partial_1 G \times (0,\, t'], \tag{15}$$

$$\frac{\partial E}{\partial n}(\mathbf{x},\, t) = -\frac{\partial E}{\partial t}(\mathbf{x},\, t), \qquad (\mathbf{x},\, t) \in \partial_1 G \times (t',\, T), \tag{16}$$

$$\frac{\partial E}{\partial n}(\mathbf{x},\, t) = -\frac{\partial E}{\partial t}(\mathbf{x},\, t), \qquad (\mathbf{x},\, t) \in \partial_2 G_T, \tag{17}$$

$$\frac{\partial E}{\partial n}(\mathbf{x},\, t) = 0, \qquad (\mathbf{x},\, t) \in \partial_3 G_T, \tag{18}$$

where $\frac{\partial}{\partial n}$ is the normal derivative. Conditions (16) and (17) are first order absorbing boundary conditions [18]. At the lateral boundaries we impose a homogeneous Neumann condition (18). In [9] it was shown that the solution to the original Maxwell's equations is well approximated by the solution to (13)–(18) in the case where $\xi = 1$ and the discontinuities in $\varepsilon_{\rm r}$ are not too large.

The model problem (13)–(18) can be also rewritten as

$$\varepsilon_{\mathrm{r}}(\mathbf{x})\frac{\partial^2 E}{\partial t^2}(\mathbf{x},\, t) + \nabla\big(\nabla\cdot E(\mathbf{x},\, t)\big) - \nabla\cdot\big(\nabla E(\mathbf{x},\, t)\big) - \xi\nabla\Big(\nabla\cdot\big(\varepsilon_{\mathrm{r}}(\mathbf{x})E(\mathbf{x},\, t)\big)\Big) = 0, \qquad (\mathbf{x},\, t)\in G\times(0,\, T), \tag{19}$$

$$E(\mathbf{x},\, 0) = 0, \quad \frac{\partial E}{\partial t}(\mathbf{x},\, 0) = 0, \qquad \mathbf{x}\in G, \tag{20}$$

$$E\,(\mathbf{x},\, t) = (0,\, f\,(t)\,,\, 0), \qquad (\mathbf{x},\, t)\in \partial_1 G\times(0,\, t']\,, \tag{21}$$

$$\frac{\partial E}{\partial n}(\mathbf{x},\, t) = -\frac{\partial E}{\partial t}(\mathbf{x},\, t), \qquad (\mathbf{x},\, t)\in \partial_1 G\times(t',\, T)\,, \tag{22}$$

$$\frac{\partial E}{\partial n}(\mathbf{x},\, t) = -\frac{\partial E}{\partial n}(\mathbf{x},\, t), \qquad (\mathbf{x},\, t)\in \partial_2 G_T, \tag{23}$$

$$\frac{\partial E}{\partial n}(\mathbf{x},\, t) = 0, \qquad (\mathbf{x},\, t)\in \partial_3 G_T. \tag{24}$$

Here we have used the well-known identity $\nabla\times(\nabla\times E) = \nabla(\nabla\cdot E) - \nabla\cdot(\nabla E)$. We refer to [9] for details of the numerical solution of the forward problem (19)–(24).

3.2 Tikhonov functional

We define Γ' as the extension of the backscattering side Γ up to the boundary $\partial_3 G$ of the domain G that is,

$$\Gamma' = \{\mathbf{x} = (x,\, y,\, z) : -X < x < X,\, -Y < y < Y,\, z = c'\}\,.$$

Let G' be the part of the rectangular prism G which lies between the two planes Γ' and $\{z = -C\}$:

$$G' = \{\mathbf{x} = (x,\, y,\, z) : -X < x < X,\, -Y < y < Y,\, -C < z < c'\}\,.$$

Denote by $Q_T = G'\times(0,\, T)$, and $S_T = \partial G'\times(0,\, T)$.

In our CIP we have the data g in (12) only on Γ. These data are complemented on the rest of the boundary $\partial G'$ of the domain G' by simulated data using the immersing procedure of [14]. Thus, we can approximately get the function $\widetilde{g}$:

$$\widetilde{g}\,(\mathbf{x},\, t) = E\,(\mathbf{x},\, t)\,, \quad (\mathbf{x}, t)\in S_T. \tag{25}$$

We solve our inverse problem as an optimization problem. To do so we minimize the Tikhonov functional:

$$F(E,\, \varepsilon_{\mathrm{r}}) := \frac{1}{2}\int_{S_T}\big(E(\mathbf{x},\, t) - \tilde{g}(\mathbf{x},\, t)\big)^2 z_\delta(t)\,\mathrm{d}\sigma\,\mathrm{d}t + \frac{1}{2}\gamma\int_G\big(\varepsilon_{\mathrm{r}}(\mathbf{x}) - \varepsilon_{\mathrm{r,\,glob}}(\mathbf{x})\big)^2\,\mathrm{d}\mathbf{x}, \tag{26}$$

where $\gamma > 0$ is the regularization parameter and $\varepsilon_{\mathrm{r,\,glob}}$ is the computed coefficient which we have obtained on the first stage via the globally convergent method. Here, $z_\delta(t)$ is used to ensure the compatibility conditions at $\overline{Q}_T\cap\{t = T\}$ for the adjoint problem, see [14] for details of this function.

Let E_{glob} be the solution of the forward problem (19)–(24) with $\varepsilon_{\mathrm{r}} := \varepsilon_{\mathrm{r,\,glob}}$. Denote by $p = \frac{\partial E_{\mathrm{glob}}}{\partial n}|_{S_T}$. In addition to the Dirichlet condition (25), we set the Neumann boundary condition as

$$\frac{\partial E}{\partial n}\,(\mathbf{x},\, t) = p\,(\mathbf{x},\, t)\,, \quad (\mathbf{x},\, t)\in S_T.$$

Introduce the following spaces of real valued vector functions

$$H^1_E(Q_T) = \big\{f\in[H^1(Q_T)]^3 : f(\mathbf{x},\, 0) = 0\big\}\,,$$

$$H^1_\lambda(Q_T) = \big\{f\in[H^1(Q_T)]^3 : f(\mathbf{x},\, T) = 0\big\}\,,$$

$$U^1 = H_E^1(G_T) \times H_\lambda^1(G_T) \times B(G),$$

where $B(G)$ is the space of functions bounded on G with the norm $\|f\|_{B(G)} = \sup_G |f|$.

To minimize the functional (26) we introduce the Lagrangian

$$\begin{aligned} L(E,\, \lambda,\, \varepsilon_{\mathrm{r}}) = F(E,\, \varepsilon_{\mathrm{r}}) &- \int_{Q_T} \varepsilon_{\mathrm{r}}(\mathbf{x}) \frac{\partial \lambda}{\partial t}(\mathbf{x},\, t) \cdot \frac{\partial E}{\partial t}(\mathbf{x},\, t)\, \mathrm{d}\mathbf{x}\, \mathrm{d}t \\ &- \int_{Q_T} \nabla \cdot E(\mathbf{x},\, t) \nabla \cdot \lambda(\mathbf{x},\, t)\, \mathrm{d}\mathbf{x}\, \mathrm{d}t + \int_{Q_T} \nabla E(\mathbf{x},\, t) \nabla \lambda(\mathbf{x},\, t)\, \mathrm{d}\mathbf{x}\, \mathrm{d}t \\ &+ \xi \int_{Q_T} \nabla \cdot \big(\varepsilon_{\mathrm{r}}(\mathbf{x}) E(\mathbf{x},\, t)\big) \nabla \cdot \lambda(\mathbf{x},\, t)\, \mathrm{d}\mathbf{x}\, \mathrm{d}t - \int_{S_T} \lambda(\mathbf{x},\, t) \cdot p(\mathbf{x},\, t)\, \mathrm{d}\sigma\, \mathrm{d}t, \end{aligned} \tag{27}$$

where E and λ are weak solutions of problems (29)–(31) and (32)–(34), respectively, see details in [14].

We observe that in (27) $(E,\, \lambda,\, \varepsilon_{\mathrm{r}}) = w \in U^1$ and functions E and λ depend on the ε_{r}. To get the Fréchet derivative L' of the Lagrangian (27) rigorously, one should assume that variations of functions E and λ depend on variations of the coefficient ε_{r}. It can be done similarly with section 4.8 of [12]. However for brevity here, to derive the Fréchet derivative of the Lagrangian (27) we assume that in (27) the elements of the vector function $(E,\, \lambda,\, \varepsilon_{\mathrm{r}})$ can be varied independently of each other.

We search for a point $w \in U^1$ such that

$$L'(w)(\overline{w}) = 0, \quad \forall \overline{w} \in U^1. \tag{28}$$

To find the Fréchet derivative $L'(w)$, we consider $L(w + \overline{w}) - L(w)$, for every $\overline{w} \in U^1$ and single out the linear part, with respect to $\overline{w}$, of the obtained expression. Then the state problem in the domain G' is given by

$$\begin{aligned} &\varepsilon_{\mathrm{r}}(\mathbf{x}) \frac{\partial^2 E}{\partial t^2}(\mathbf{x},\, t) + \nabla\big(\nabla \cdot E(\mathbf{x},\, t)\big) \\ &\qquad - \nabla \cdot \big(\nabla E(\mathbf{x},\, t)\big) - \xi \nabla\Big(\nabla \cdot \big(\varepsilon_{\mathrm{r}}(\mathbf{x}) E(\mathbf{x},\, t)\big)\Big) = 0, && (\mathbf{x},\, t) \in Q_T, \end{aligned} \tag{29}$$

$$E(\mathbf{x},\, 0) = 0, \quad \frac{\partial E}{\partial t}(\mathbf{x},\, 0) = 0, \qquad \mathbf{x} \in G', \tag{30}$$

$$\frac{\partial E}{\partial n}(\mathbf{x},\, t) = p(\mathbf{x}, t), \qquad (\mathbf{x},\, t) \in S_T. \tag{31}$$

The adjoint problem is:

$$\begin{aligned} &\varepsilon_{\mathrm{r}}(\mathbf{x}) \frac{\partial^2 \lambda}{\partial t^2}(\mathbf{x},\, t) + \nabla\big(\nabla \cdot \lambda(\mathbf{x},\, t)\big) \\ &\qquad - \nabla \cdot \big(\nabla \lambda(\mathbf{x},\, t)\big) - \xi \varepsilon_{\mathrm{r}}(\mathbf{x}) \nabla\big(\nabla \cdot \lambda(\mathbf{x},\, t)\big) = 0, && (\mathbf{x},\, t) \in Q_T, \end{aligned} \tag{32}$$

$$\lambda(\mathbf{x},\, T) = 0, \quad \frac{\partial \lambda}{\partial t}(\mathbf{x},\, T) = 0, \qquad \mathbf{x} \in G', \tag{33}$$

$$\frac{\partial \lambda}{\partial t}(\mathbf{x},\, t) = z_\delta(t) \big(\widetilde{g}(\mathbf{x},\, t) - E(\mathbf{x},\, t)\big)(\mathbf{x}, t), \qquad (\mathbf{x},\, t) \in S_T. \tag{34}$$

4 Finite element discretization

For the finite element discretization of $\Omega_T = \Omega \times (0, T)$ we used stabilized finite element method of [9]. To do that we define a partition $K_h = \{K\}$ of G' which consists of tetrahedra. Here h is a mesh function defined as $h|_K = h_K$ – the local diameter of the element K. Let $J_\tau = \{J\}$ be a partition of the time interval $(0,\, T)$ into subintervals $J = (t_{k-1},\, t_k]$ of uniform length $\tau = t_k - t_{k-1}$. We also assume the minimal angle condition on the K_h [15].

To solve the state problem (29)–(31) and the adjoint problem (32)–(34) we define the finite element spaces, $W_h^E \subset H_E^1(Q_T)$ and $W_h^\lambda \subset H_\lambda^1(Q_T)$. First, we introduce the finite element trial space W_h^E for every component of the electric field E defined by

$$W_h^E := \{w \in H_E^1(Q_T) : w|_{K\times J} \in P_1(K) \times P_1(J),\ \forall K \in K_h,\ \forall J \in J_\tau\},$$

where $P_1(K)$ and $P_1(J)$ denote the set of linear functions on K and J, respectively. We also introduce the finite element test space W_h^λ defined by

$$W_h^\lambda := \{w \in H_\lambda^1(Q_T) : w|_{K\times J} \in P_1(K) \times P_1(J),\ \forall K \in K_h,\ \forall J \in J_\tau\}.$$

Hence, the finite element spaces W_h^E and W_h^λ consist of continuous piecewise linear functions in space and time. To approximate the function ε_{r}, we use the space of piecewise constant functions $V_h \subset L_2(\Omega)$,

$$V_h := \{u \in L_2(\Omega) : u|_K \in P_0(K),\ \forall K \in K_h\},$$

where $P_0(K)$ is the set of constant functions on K.

Next, we set $U_h = W_h^E \times W_h^\lambda \times V_h$. The finite element method for solving equation (28) now reads: *Find $u_h \in U_h$, such that*

$$L'(u_h)(\bar{u}) = 0,\ \forall \bar{u} \in U_h.$$

5 General framework for a posteriori error estimation for CIPs

Let $(E_h,\, \lambda_h,\, \varepsilon_h) \in U_h$ be finite element approximations of functions $(E,\, \lambda,\, \varepsilon_{\mathrm{r}}) \in U^1$, see details in [9, 10]. In our recent works [7, 11, 12] we derived a posteriori error estimates for three kinds of errors:

- The error $|L(u) - L(u_h)|$ in the Lagrangian with $u = (E,\, \lambda,\, \varepsilon_{\mathrm{r}})$, and $u_h = (E_h,\, \lambda_h,\, \varepsilon_h)$. This error for hyperbolic CIPs was presented in [7, 11].
- The error $|F(\varepsilon_{\mathrm{r}}) - F(\varepsilon_h)|$ in the Tikhonov functional. This error for hyperbolic CIPs was derived in [12].
- The error $|\varepsilon_{\mathrm{r}} - \varepsilon_h|$ in the regularized solution of this functional ε_{r}. This error for hyperbolic CIPs was presented in [12].

To derive errors in the Lagrangian or in the Tikhonov functional we first note that

$$\begin{aligned} L(u) - L(u_h) &= L'(u_h)(u - u_h) + R(u,\, u_h), \\ F(\varepsilon_{\mathrm{r}}) - F(\varepsilon_h) &= F'(\varepsilon_h)(\varepsilon_{\mathrm{r}} - \varepsilon_h) + R(\varepsilon_{\mathrm{r}},\, \varepsilon_h), \end{aligned} \tag{35}$$

where $R(u,\, u_h)$,and $R(\varepsilon_{\mathrm{r}},\, \varepsilon_h)$ are the second order remainders terms. We assume that ε_h is located in the small neighborhood of ε_{r}. Thus, the terms $R(u,\, u_h)$, $R(\varepsilon_{\mathrm{r}},\, \varepsilon_h)$ are small and we can neglect them in (35).

We now use the Galerkin orthogonality principle

$$\begin{aligned} L'(u_h)(\bar{u}) &= 0 \quad \forall \bar{u} \in U_h, \\ F'(\varepsilon_h)(b) &= 0 \quad \forall b \in V_h, \end{aligned}$$

together with the splitting

$$\begin{aligned} u - u_h &= (u - u_h^{\mathrm{I}}) + (u_h^{\mathrm{I}} - u_h), \\ \varepsilon_{\mathrm{r}} - \varepsilon_h &= (\varepsilon_{\mathrm{r}} - \varepsilon_h^{\mathrm{I}}) + (\varepsilon_h^{\mathrm{I}} - \varepsilon_h), \end{aligned}$$

where $u_h^{\mathrm{I}} \in U_h$ is the interpolant of u, and $\varepsilon_h^{\mathrm{I}} \in V_h$ is the interpolant of ε_{r}, and get the following representation of errors in the Lagrangian and in the Tikhonov functional, respectively:

$$\begin{aligned} L(u) - L(u_h) &\approx L'(u_h)(u - u_h^{\mathrm{I}}), \\ F(\varepsilon_{\mathrm{r}}) - F(\varepsilon_h) &\approx F'(\varepsilon_h)(\varepsilon_{\mathrm{r}} - \varepsilon_h^{\mathrm{I}}). \end{aligned} \tag{36}$$

In the a posteriori error estimates (36) we have two types of "factors":

- $L'(u_h)$ and $F'(\varepsilon_h)$ represent *residuals*, and
- $u - u_h^{\mathrm{I}}$ and $\varepsilon_{\mathrm{r}} - \varepsilon_h^{\mathrm{I}}$ represent *weights*.

The residuals of (36) can be computed by knowing the finite element approximations (E_h, λ_h, ε_h), but the weights must be further estimated.

Let $f \in H^1(\Omega)$ be approximated by its piecewise linear interpolant f_h^{I} and finite element approximation f_h over a mesh K_h of Ω as outlined in Section 4. Standard interpolation estimates (following from, for instance, [19]) then gives

$$\left\| f - f_h^{\mathrm{I}} \right\|_{L_2(\Omega)} \leq C_{\mathrm{I}} \left\| h \, \nabla f \right\|_{L_2(\Omega)}. \tag{37}$$

where $C_{\mathrm{I}} = C_{\mathrm{I}}(\Omega, h)$ is positive constant depending only on the domain Ω and the mesh function $h = h(x)$, the latter defined as in Section 4. In addition, we can estimate right hand side in (37), see [19], via

$$|\nabla f| \leq \frac{|[f_h]|}{h_K}, \tag{38}$$

where $[f_h]$ denotes the normal jump of the function f_h over the edges of the element K.

Similarly with (37), (38) we estimate $u - u_h^{\mathrm{I}}$ in terms of derivatives of the function u and the mesh parameters h and τ as

$$|u - u_h^{\mathrm{I}}| \leq C_{\mathrm{I}} \left(h^2 \left| \frac{[u_h]_{\mathrm{s}}}{h} \right| + \tau^2 \left| \frac{[u_h]_{\mathrm{t}}}{\tau} \right| \right), \tag{39}$$

where $[u_h]_{\mathrm{s}}$ is the maximum modulus of a jump in the normal derivative of u_h across a side of the element K, $[u_h]_{\mathrm{t}}$ is the maximum modulus of the jump of the time derivative of u_h across a boundary node of the time interval J, see details in [7, 8, 10, 11].

We also estimate $\varepsilon_{\mathrm{r}} - \varepsilon_h^{\mathrm{I}}$ in terms of derivatives of the function ε_{r} and the mesh parameter h as

$$|\varepsilon_{\mathrm{r}} - \varepsilon_h^{\mathrm{I}}| \leq C_{\mathrm{I}} h \left| \frac{[\varepsilon_h]}{h} \right|. \tag{40}$$

Here, $[\varepsilon_h]$ is the jump of the function ε_h over the element K. Substituting estimates (39) and (40) in the right hand side of (36) we can compute a posteriori errors in the Lagrangian or in the Tikhonov functional in explicit way as

$$\begin{aligned} |L(u) - L(u_h)| &\approx C_{\mathrm{I}} ||L'(u_h)|| \cdot (h||[u_h]_{\mathrm{s}}|| + \tau||[u_h]_{\mathrm{t}}||), \\ |F(\varepsilon_{\mathrm{r}}) - F(\varepsilon_h)| &\approx C_{\mathrm{I}} ||F'(\varepsilon_h)|| \cdot |||[\varepsilon_h]|||. \end{aligned}$$

Finally, to derive an estimate for the error $\varepsilon_{\mathrm{r}} - \varepsilon_h$ in the regularized solution ε_{r} we use the convexity property of the Tikhonov functional together with the interpolation property (37). Below we formulate theorem of [12] for the case of a posteriori error estimate in the reconstructed function ε_{r} for the problem (1)–(2).

Theorem [12] *Let $\varepsilon_h \in V_h$ be a finite element approximation of the solution $\varepsilon_{\mathrm{r}} \in H^1(\Omega)$ on the finite element mesh K_h with the mesh function h. Then there exists a constant D such that $\|F'(\varepsilon_1) - F'(\varepsilon_2)\| \leq D \|\varepsilon_1 - \varepsilon_2\|$ for every ε_1, ε_2 satisfying* (3)*. Then the following a posteriori error estimate for the regularized solution ε_{r} holds*

$$||\varepsilon_h - \varepsilon_{\mathrm{r}}||_{L^2(\Omega)} \leq \frac{D}{\alpha} C_I ||h\varepsilon_h||_{L_2(\Omega)}.$$

Remark 5.1. The natural question linked with the adaptivity is: Can one rigorously guarantee that the mesh obtained after the minimization of the Tikhonov functional on sequentially refined meshes of finite elements results in an improvement of the accuracy? For the first time this question was answered positively in [6], also, see the book [12] and the survey [26].

6 Mesh refinement recommendation and the adaptive algorithm

In our adaptive algorithm for the mesh refinement we have used ideas of [11] and the Theorem 5.1 and criterion of the Remark 5.1 of [10]. From this criterion follows that the finite element mesh should be locally refined in such subdomain of Ω where the maximum norm of the Fréchet derivative of the objective functional is large.

Define

$$L_h'^{,m}(\mathbf{x}) = -\int_0^T \frac{\partial \lambda_h^m}{\partial t}(\mathbf{x},\, t) \cdot \frac{\partial E_h^m}{\partial t}(\mathbf{x},\, t)\, \mathrm{d}t + \xi \int_0^T \nabla \cdot E_h^m(\mathbf{x},\, t) \nabla \cdot \lambda_h^m(\mathbf{x},\, t)\, \mathrm{d}t + \gamma(\varepsilon_h{}^m(\mathbf{x}) - \varepsilon_{\mathrm{r,\,glob}}(\mathbf{x})), \tag{41}$$

where m is the iteration index in the optimization procedure, and $(E_h^m,\, \lambda_h^m,\, \varepsilon_h^m)$ are finite element approximations of the functions $(E,\, \lambda,\, \varepsilon_{\mathrm{r}})$, see details in [9, 10].

Adaptive algorithm

- Step 0. Choose an initial mesh K_h in Ω and an initial time partition J_0 of the time interval $(0,\, T)$. Start from the initial guess $\varepsilon_h^0 = \varepsilon_{\mathrm{r,\,glob}}$. Compute the approximations ε_h^m as:
- Step 1. Compute the approximate solutions E_h^m and λ_h^m of the state problem (19)–(22) and the adjoint problem (32)–(34) on K_h and J_k, using coefficient ε_h^m, and compute the Fréchet derivative $L_h'^{,m}$ via (41).
- Step 2. Update the coefficient on K_h using the conjugate gradient method:

  $$\varepsilon_h^{m+1}(\mathbf{x}) := \varepsilon_h^m(\mathbf{x}) + \alpha d^m(\mathbf{x}),$$

  where $\alpha > 0$ is a step-size in the conjugate gradient method, and

  $$d^m(\mathbf{x}) = -L_h'^{,m}(\mathbf{x}) + \beta^m d^{m-1}(\mathbf{x}),$$

  with

  $$\beta^m = \frac{||L_h'^{,m}||^2_{L_2(\Omega)}}{||L_h'^{,m-1}||^2_{L_2(\Omega)}},$$

  and $d^0(\mathbf{x}) = -L_h'^{,0}(\mathbf{x})$.
- Step 3. Stop updating the coefficient and set $\varepsilon_h := \varepsilon_h^{m+1}$, $M := m+1$, if either $||L_h'^{,m}||_{L_2(\Omega)} \le \theta$ or norms $||\varepsilon_h^m||_{L_2(\Omega)}$ are stabilized. Here θ is a tolerance number. Otherwise, set $m := m+1$ and go to step 1.
- Step 4. Compute $L_h'^{,M}$ via (41). Refine the mesh at all grid points $\mathbf{x}$ where

  $$|L_h'^{,M}(\mathbf{x})| \ge \beta_1 \max_{\mathbf{x} \in \overline{\Omega}} |L_h'^{,M}(\mathbf{x})|.$$

  Here the tolerance number $\beta_1 \in (0,\, 1)$ is chosen by the user.
- Step 5. Construct a new mesh K_h in Ω and a new partition J_k of the time interval $(0,\, T)$. On J_k the new time step τ should be chosen in such a way that the CFL condition is satisfied. Interpolate the initial approximation $\varepsilon_{\mathrm{r,\,glob}}$ from the previous mesh to the new mesh. Next, return to step 1 at $m = 1$ and perform all above steps on the new mesh. Stop mesh refinements if norms defined in step 3 either increase or stabilize, compared with the previous mesh.

In step 2 of this algorithm α can be computed by a line search procedure, see, for example, [23].

7 Numerical studies

In this section we present results of reconstruction of buried objects placed inside a sand box using the two-stage numerical procedure. To do that we use the approximate globally convergent algorithm of section 2 on the first stage and the adaptive algorithm of section 6 on the second stage.

To collect experimental data we have used the same configuration as for the targets placed in the air, see [13, 21] for details. The only difference is that in this work we consider the objects placed inside a box filled with dry sand. The relative dielectric constant of dry sand is $\varepsilon_{\mathrm{r}}\left(\text{sand}\right) = 4$. We used this information to model the case of buried objects. In our experiment we have used different types of targets, including both metallic and nonmetallic ones. We refer to the Table 5.1 of [22] for the full description of all data sets. In this paper we present reconstruction of four targets listed in the Table 1. We refer to [22] for details of the data acquisition process.

In our computational studies we had the following goals:

- to reconstruct refractive indices of dielectric targets and appearing dielectric constants of metals, and
- to image the location of targets, and their sizes and shapes.

To work with metallic objects, it is convenient to treat them as dielectrics with large dielectric constants, see [20] for details. We call these *appearing dielectric constants* and choose values for them in the interval

$$\varepsilon_{\mathrm{r}}\left(\text{metallic target}\right) \in (10,\, 25)\,. \tag{42}$$

Using (42), we set in all our tests the upper value of the function ε_{r} as $b = 25$, see (3). Thus, we set lower and upper bounds for the reconstructed function ε_{r} in Ω as

$$M_{\varepsilon_{\mathrm{r}}} = \{\varepsilon_{\mathrm{r}}(\mathbf{x}) : \varepsilon_{\mathrm{r}}\left(\mathbf{x}\right) \in [1,\, 25]\,,\ \mathbf{x} \in \Omega\}. \tag{43}$$

We ensure the upper bound in (43) via truncating to 25 those values of ε_{r} which exceed this number. Similarly we deal with the lower bound of (43).

To compare our computational results with directly measured refractive indices $n = \sqrt{\varepsilon_{\mathrm{r}}}$ of dielectric targets and effective dielectric constants of metallic targets (see (42)), we consider the maximal values of the computed functions ε_{r} obtained in both algorithms, and define

$$\varepsilon_{\mathrm{r}}^{\mathrm{comp}} = \max_{\mathbf{x}\in\overline{\Omega}} \varepsilon_{\mathrm{r}}\left(\mathbf{x}\right), \quad n^{\mathrm{comp}} = \sqrt{\varepsilon_{\mathrm{r}}^{\mathrm{comp}}}. \tag{44}$$

Remark 7.1. As the objects we reconstruct are buried in dry sand with relative dielectric constant 4, our computational results should be scaled by that factor in order to obtain correct apparent dielectric constants and refractive indices. In Tables 2–5, we present such scaled results.

7.1 Data preprocessing

We point out that there is a *huge misfit* between our experimental data and computationally simulated data. There are several causes of this misfit listed in Section 4.2 of [21]. Because of this misfit, the *central procedure* required before applying of our two-stage numerical procedure is data preprocessing. This procedure is heuristic and cannot be rigorously justified. In this work we have used the same data preprocessing procedure consisting of several steps as was used in [21, 22]. The three main steps in this data preprocessing are:

1. Data propagation.
2. Extraction of the targets signal from the total signal, which is a mixture of the signal from the target and the signal from the sand. This extraction is applied to propagated data.

3. Data calibration: to scale the measured data to the same scaling as in our simulations. In the case of the globally convergent method, a calibrating object was used. In the case of the above described adaptive finite element method a different calibration was used, see for details [14].

We have propagated the data to a plane, which we call as the *propagated plane* and is located closer to the targets. This means that we approximate the scattered wave on the propagated plane using the measured scattered wave on the measurement plane. The distance between the measurement plane and the target was found using first time of arrival of the backscattered signal. Data calibration is used to scale the measured data by a certain factor obtained in our simulations. We call this factor the *calibration factor*. The choice of this factor is based on the data of a known target which we call the *calibrating object*. The procedure of the extraction of the signal of the target from the total signal is more complicated and we refer to [22] for its many details.

7.2 Computational domains

We choose our computational domain G as

$$G = \{\mathbf{x} =(x,\, y,\, z) \in (-0.56,\, 0.56) \times (-0.56,\, 0.56) \times (-0.16,\, 0.1)\}\,. \tag{45}$$

The boundary of the domain G is $\partial G = \partial_1 G \cup \partial_2 G \cup \partial_3 G$. Here, $\partial_1 G$ and $\partial_2 G$ are front and back sides of the domain G at $\{z = 0.1\}$ and $\{z = -0.16\}$, respectively, and $\partial_3 G$ is the union of left, right, top and bottom sides of this domain.

The the domain G is split into two subdomains $\Omega_{\text{FEM}} = \Omega$ and Ω_{FDM} so that $G = \Omega_{\text{FEM}} \cup \Omega_{\text{FDM}}$ and inner domain is defined as

$$\Omega_{\text{FEM}} = \Omega = \{\mathbf{x} =(x,\, y,\, z) \in (-0.5,\, 0.5) \times (-0.5,\, 0.5) \times (-0.1,\, 0.04)\}\,. \tag{46}$$

The experimental data g for both algorithms are given at the front side Γ of the domain Ω which is defined as

$$\Gamma = \{\mathbf{x} = (x,\, y,\, z) \in \partial\Omega : z = 0.04\}$$

In some tests of the first stage we used the shrunken computational domain G defined as

$$G = \{\mathbf{x} =(x,\, y,\, z) \in (-0.24,\, 0.24) \times (-0.24,\, 0.24) \times (-0.16,\, 0.1)\}\,,$$

as well as the shrunken computational domain Ω_{FEM} defined as

$$\Omega_{\text{FEM}} = \Omega = \{\mathbf{x} =(x,\, y,\, z) \in (-0.2,\, 0.2) \times (-0.2,\, 0.2) \times (-0.1,\, 0.04)\}\,. \tag{47}$$

7.3 Description of experimental data sets

To test performance of both stages we have applied first the approximate globally convergent algorithm and then an adaptive finite element method to reconstruct the targets presented in Table 1. This table describes the details of used data sets together with the burial depths of the targets. After obtaining computational results the refractive indices of all dielectric targets were measured, and these measured refractive indices were compared to those predicted by the computations.

Some of the non-blind targets were used for the calibrating procedure. The blind targets were used to ensure that our two-stage procedure works in realistic blind data cases.

We note that the burial depths of the targets of Table 1 varied between 3 cm to 5 cm. Typically burial depths of antipersonnel land mines do not exceed 10 cm. The measured data of the sand box (without buried objects) was used for the calibration of all data for the four objects of Table 1.

7.4 Numerical examples of the first stage

In Tables 2 and 3 we summarize reconstruction results for all objects of Table 1. Table 2 shows shows the reconstructed refractive indices for the non-metallic targets. For these targets, the refractive index $n = \sqrt{\varepsilon_{\rm r}(\text{target})}$. Here, $\varepsilon_{\rm r}(\text{target})$ was chosen as $\varepsilon_{\rm r}(\text{target}) = \max_{\mathbf{x}\in\Omega} \varepsilon_{\rm r}(\mathbf{x})$. Table 3 shows the burial depths and the effective dielectric constants of the metallic targets. From Tables 2 and 3 we can see that the burial depth was accurately estimated in most cases, with the errors not exceeding 1 cm.

The estimates of the refractive indices of non-metallic targets with refractive indices larger than that of the sand (water and wet wood) are quite accurate with the average error of about 8.5%.

Note that the error in our direct measurement of the refractive index of the wet wood was 10%. For water, we were unable to directly measure its refractive index at the used frequency of the signal, which was about 7.5 GHz. Therefore, we have made a separate experiment described in [22] where we have obtained a reference value $n = 4.88$ for water. We observe from Table 2 that for water we have obtained a value of n close to the reference value. Targets with smaller refractive indices than that of the sand are modelling plastic land mines and improvised explosive devices (IEDs). We have observed that in this case we can image these targets only if their burial depths do not exceed 5 cm, see for example, reconstruction of target 3 in Table 2 and in Figure 2-c).

In our experiments we observed that the signals of the metallic targets were stronger compared to the signal from sand. In our previous works, we have established that the effective dielectric constant of metals should be larger than 10–15, see [13, 21]. From Table 3 we see that we have obtained similar results as in our previous studies.

From Table 1 we observe that in our experiments we were supposed to reconstruct two metallic blocks which were placed at 1 cm separation to each other. On the other hand, the wavelength λ of our device is 4.5 cm. Thus, $\lambda/4.5$ is the distance between these two targets and *superresolution* is achieved beyond the diffraction limit. Table 3 and Figure 2-d) shows that we have accurately imaged both targets. This phenomenon was not expected and should be studied further because of its importance when combined with quantitative imaging.

7.5 Numerical examples of the second stage

From the results of the first stage we can conclude that this stage provides accurate locations of the targets as well as accurate values of the refractive indices $n = \sqrt{\varepsilon_{\rm r}}$ of the dielectric targets and large values of effective dielectric constants $\varepsilon_{\rm r}$ for the metallic targets of interest. However, the approximate globally convergent algorithm does not reconstruct the shapes of the targets in the z-direction well, see Figure 2. Because of that we have used the second stage where we have minimized the Tikhonov functional on locally adaptively refined meshes.

7.5.1 Computations of the forward problem

The data g in our experiments of the second stage are given only for the second component E_2 of the electric field E in (12) and are measured at the front side Γ of the domain Ω which is defined as

$$\Gamma = \{\mathbf{x} = (x,\, y,\, z) \in \partial\Omega : z = 0.04\}.$$

To generate backscattering data for other two components E_1 and E_3 we solve the forward problem (19)–(24) in the computational domain G defined as in the first stage in (45) with the known value of $\varepsilon_{\rm r}$ obtained at the first stage of our two-stage numerical procedure. We use a stabilized domain decomposition method of [9] implemented in the software package WavES [25]. We split G into two subdomains $\Omega_{\rm FEM} = \Omega$ and $\Omega_{\rm FDM}$ so that $G = \Omega_{\rm FEM} \cup \Omega_{\rm FDM}$ and the inner domain is defined as in (46).

Once the forward problem (19)–(24) is solved to generate backscattering data for the two components E_1 and E_3 at the boundary Γ', then after the data immersing procedure described in Section 7.3.3 of [14] the inverse problem is solved via the algorithm of section 6. The immersing procedure of [14] immerses the time-dependent propagated experimental data $g\,(\mathbf{x},\, t) = E_2\,(\mathbf{x},\, t)|_{\mathbf{x}\in\Gamma}$ into the computationally simulated data and then extends the data g from Γ to Γ'.

Object #	Blind/ Non-blind	Description of target	Material
1	Non-blind	A metallic ball, 3 cm burial depth	Metal
2	Non-blind	A bottle filled with clear water, 3 cm depth	Water
3	Blind	A ceramic mug, 5 cm burial depth	Ceramic
4	Non-blind	Two metallic blocks at 1 cm separation	Metal/Metal

Table 1: *Description of the data sets.*

We choose the waveform f in (19)–(24) as

$$f(t) = \sin(\omega t), \quad 0 \leq t \leq t' := \frac{2\pi}{\omega},$$

where we use $\omega = 30$ and $T = 1.2$. We solve the problem (19)–(24) using the explicit scheme of [9] with the time step size $\tau = 0.003$, which satisfies the CFL condition.

7.5.2 Reconstructions

Suppose that in the adaptive algorithm of section 6 we have obtained the function ε_{r}. We obtain then the image of the dielectric targets based on the function $\varepsilon_{\mathrm{r,\,diel}}$ which we define as

$$\varepsilon_{\mathrm{r,\,diel}}(\mathbf{x}) = \begin{cases} \varepsilon_{\mathrm{r}}(\mathbf{x}) \ \text{ if } \varepsilon_{\mathrm{r}}(\mathbf{x}) \geq 0.5 \max_{\mathbf{x}\in\overline{\Omega}} \varepsilon_{\mathrm{r}}(\mathbf{x}), \\ 1 \text{ otherwise.} \end{cases}$$

For metallic targets we used similar function $\varepsilon_{\mathrm{r,\,metal}}$,

$$\varepsilon_{\mathrm{r,\,metal}}(\mathbf{x}) = \begin{cases} \varepsilon_{\mathrm{r}}(\mathbf{x}) \ \text{ if } \varepsilon_{\mathrm{r}}(\mathbf{x}) \geq 0.5 \max_{\mathbf{x}\in\overline{\Omega}} \varepsilon_{\mathrm{r}}(\mathbf{x}), \\ 1 \text{ otherwise.} \end{cases}$$

In our experiments we apply the adaptive algorithm of section 6 to improve shape of targets listed in Table 1.

Recall that to apply immersing procedure of the experimental data g into simulated data E_2 we solve the problem (19)–(24) numerically with the known values of the function $\varepsilon_{\mathrm{r}} = \varepsilon_{\mathrm{r,\,glob}}$ obtained at the first stage of our two-stage numerical procedure, see Tables 2, 3 for the function $\varepsilon_{\mathrm{r,\,glob}}$. Figure 1 show backscattering immersed data of the second component of electric field E_2 for target #4 (two metallic blocks) of Table 1 at different times.

Table 4 lists both computed refractive index n^{comp}, obtained via (44), on adaptively refined meshes and directly measured refractive indices n of the dielectric targets. Table 5 lists calculated appearing dielectric constants $\varepsilon_{\mathrm{r}}^{\mathrm{comp}}$ of the metallic targets. From Table 5 we observe that $\varepsilon_{\mathrm{r}}^{\mathrm{comp}} > 10$ for all metallic targets, and thus (42) is satisfied.

An important observation, which can be deduced from Table 5, is that our adaptive algorithm can still compute large inclusion/background contrasts exceeding 10:1.

Figures 3–7 display adaptively refined meshes and 3D images of some targets of Table 1. To have a better visualization, we have zoomed some figures from the domain Ω_{FEM} defined in (46) to the domain defined in (47). We can conclude that the location of all targets as well as their sizes in the x-, y-, and z-directions are well estimated on the second stage of our two-stage numerical procedure.

Object #	Material	Computed depth	Exact depth	Computed n	Measured n
2	Water	3.6	4.0	4.7	4.88
3	Ceramic	4.0	5.0	1.0	1.39

Table 2: *Result of the first stage: the refractive indices* $n = \sqrt{\varepsilon_{\rm r}}$ *and the burial depths of non-metallic targets.*

Object #	Material	Computed depth	Exact depth	Computed $\varepsilon_{\rm r}$
1	Metal	2.9	3.0	31.0
4	Metal	3.8	4.0	99.8
	Metal	4.0	4.0	56.5

Table 3: *Result of the first stage: the estimated effective dielectric constants and the burial depths of metallic targets. Object #4 consists of two metallic targets with 1 cm distance between their surfaces.*

Target number	2	3
blind (yes/no)	no	no
Measured n	4.88	1.39
$n^{\rm comp}$ coarse mesh	4.7	1
$n^{\rm comp}$ 1 time ref. mesh	4.7	1
$n^{\rm comp}$ 2 times ref.mesh	4.7	1
$n^{\rm comp}$ 3 times ref.mesh	4.7	1

Table 4: *Stage 2. Computed* $n^{\rm comp}$ *and directly measured* n *refractive indices of dielectric targets.*

Target number	1	4
blind (yes/no)	no	no
$\varepsilon_{\rm r}^{\rm comp}$ coarse mesh	24.5	75.6
$\varepsilon_{\rm r}^{\rm comp}$ 1 time ref. mesh	24.6	100
$\varepsilon_{\rm r}^{\rm comp}$ 2 times ref.mesh	24.7	100
$\varepsilon_{\rm r}^{\rm comp}$ 3 times ref.mesh	24.6	100

Table 5: *Stage 2. Computed appearing dielectric constants* $\varepsilon_{\rm r}^{\rm comp}$ *of metallic targets.*

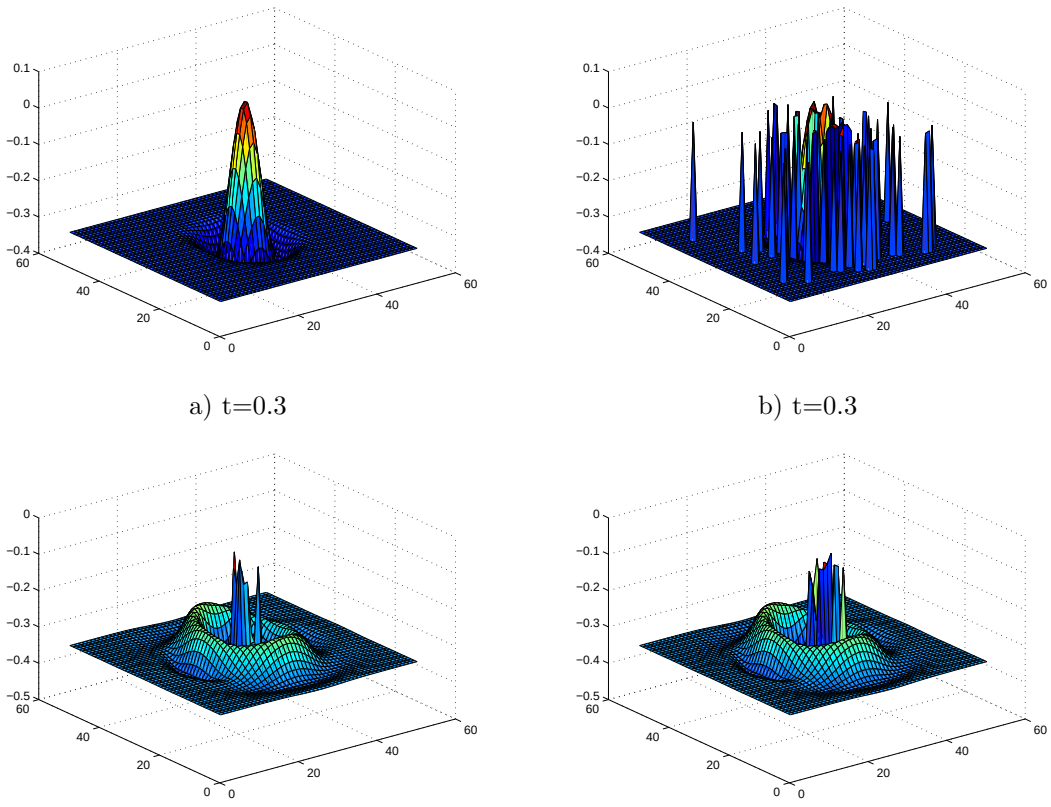

a) t=0.3 b) t=0.3

c) t=0.45 d) t=0.45

Figure 1: Backscattering immersed data of the second component E_2 of the electric field for object 4 (two metallic blocks at 1 cm separation) of Table 1. On the left we show backscattering immersed data which are immersed into measured data without presence of sand, on the right - with presence of sand. Recall that the final time is $T = 1.2$.

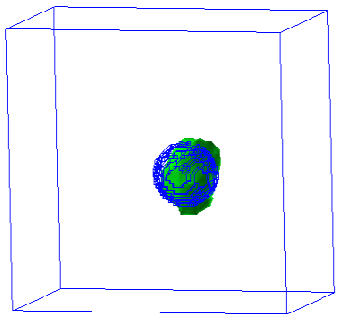

a) target 1

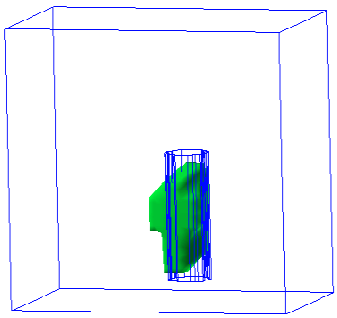

b) target 2

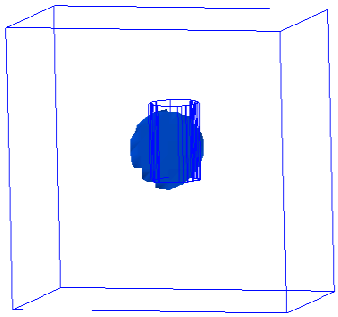

c) target 3

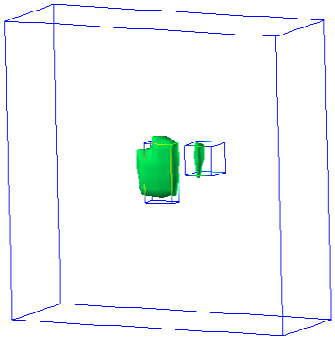

d) targets 4

Figure 2: *Reconstructions of targets of Table 1 obtained on the first stage of our two-stage numerical procedure.*

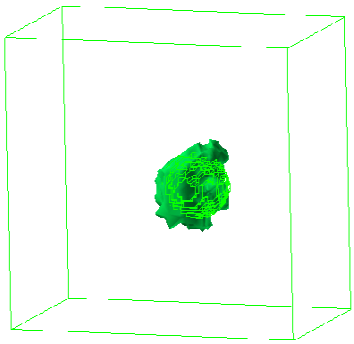

a) three times refined mesh, xy-view

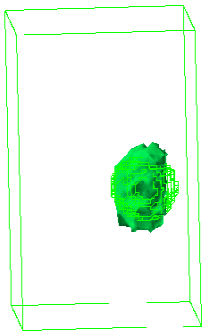

b) three times refined mesh, yz-view

Figure 3: *Computed image of target number 1 of Table 1 . Thin lines indicate correct shape. To have a better visualization we have zoomed the domain Ω in (46) in the domain Ω_{FEM} in (47).*

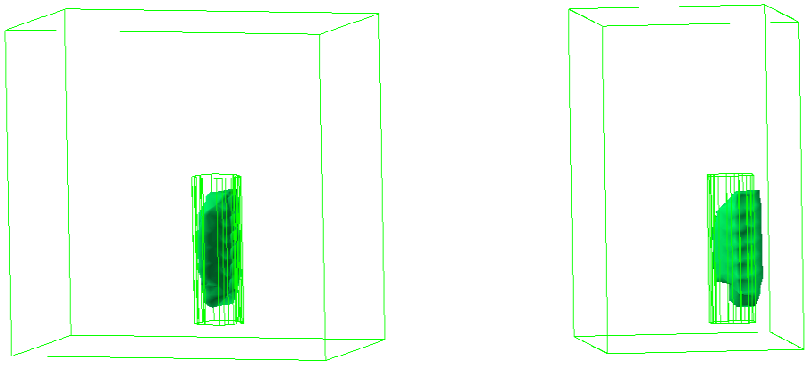

a) twice refined mesh, xy-view b) twice refined mesh, yz-view

Figure 4: *Computed image of target number 2 of Table 1 . Thin lines indicate correct shape. To have a better visualization we have zoomed the domain Ω in (46) in the domain Ω_{FEM} in (47). This target, which was a plastic bottle filled with water, was quite a large vertical size of 20 cm. On the other hand, our incident signal had a low power, which was much lower at the top and bottom of this target. This is why we were unable to image well the vertical size of this target. Still, one can observe that the image is stretched in the vertical direction.*

8 Summary

This is the fifth (5th) paper (after [13, 14, 21, 22]) in the recent series of publications of this group about the performance of the two-stage numerical procedure of [12] on experimental backscattering time-dependent data generated by a single location of the source of electromagnetic waves. While in [13, 14, 21] we have considered the case of targets placed in air, in [22] and here we consider the more challenging case of targets buried in the ground. This case is more challenging because the signal scattered by the ground is heavily mixed with the signal scattered by the target.

It was shown in [22] that the globally convergent numerical method of [12] accurately images refractive indices and locations of buried targets. In this paper we complement the globally convergent method by the locally convergent adaptivity technique. The adaptivity takes the image of the globally convergent method as the starting point for subsequent iterations. The theory of the adaptivity can be found in [2, 3, 4, 5, 6, 7, 8], [10, 11, 12], and [26]. In particular, the important analytical guarantee of the fact that adaptivity indeed refines images was first established in [6] and then also published in [12] and [26].

As a result of the application of the adaptivity, our images are significantly refined: the shapes of the targets are accurately imaged. A particularly interesting case is the case of the superresolution (Figure 2-d and Figures 5). We have accurately imaged both targets in this case.

In conclusion, we believe that the two-stage numerical procedure of [12] is now completely verified on experimental data.

Acknowledgments

This research was supported by US Army Research Laboratory and US Army Research Office grant W911NF-11-1-0399, the Swedish Research Council, the Swedish Foundation for Strategic Research (SSF) through the Gothenburg Mathematical Modelling Centre (GMMC). The computations were performed on resources at Chalmers Centre for Computational Science and Engineering (C3SE) provided by the Swedish National Infrastructure for Computing (SNIC).

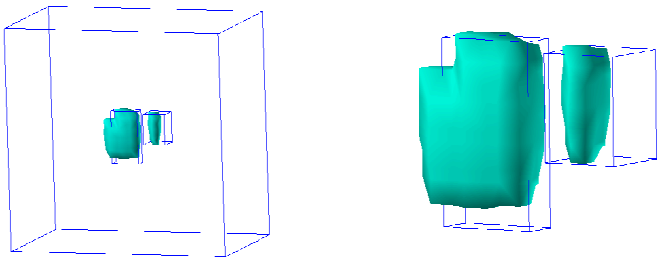

a) coarse mesh b) zoomed view

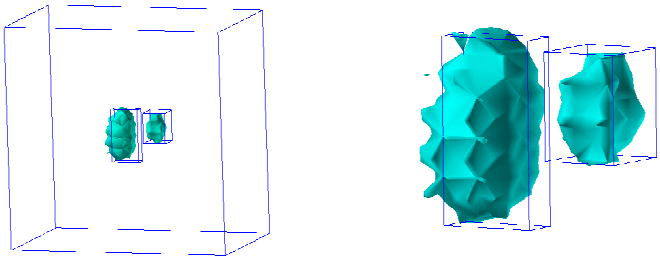

c) two times refined mesh d) zoomed view

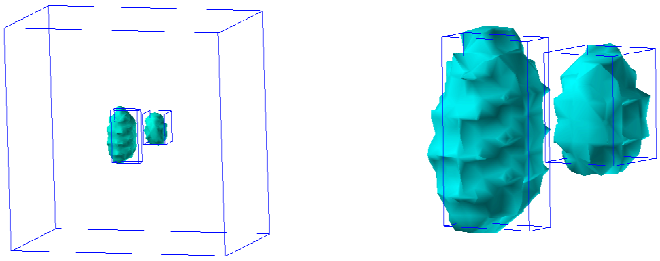

e) three times refined mesh f) zoomed view

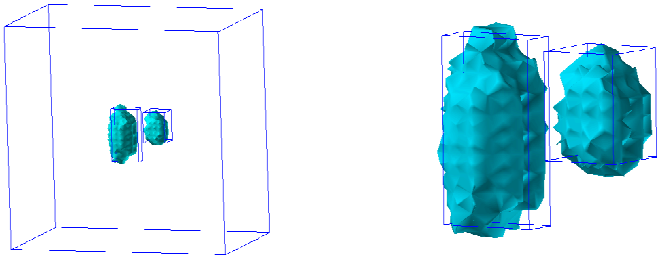

g) four times refined mesh h) zoomed view

Figure 5: *Computed images of targets number 4 of Table 1 when superresolution is achieved on four times adaptively refined meshes. Compare with Figure 2-d).*

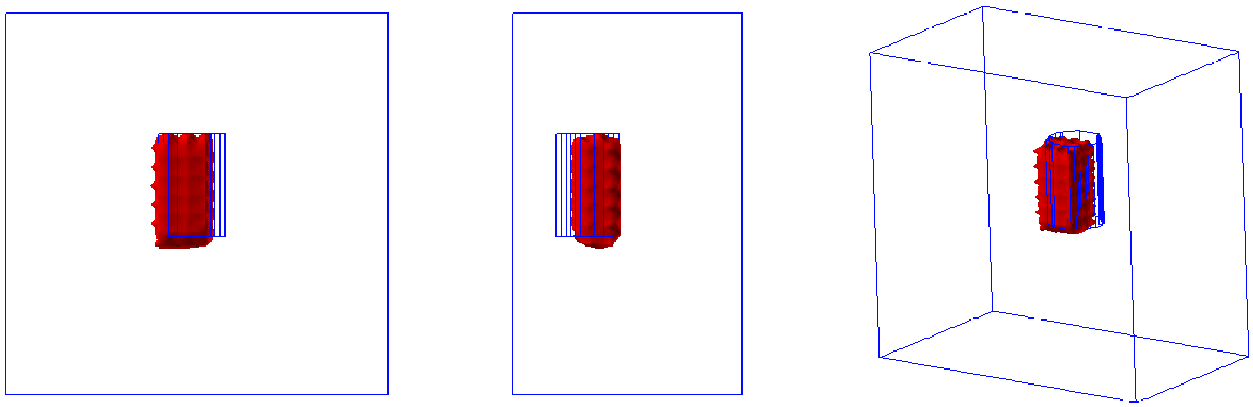

(a) Front (b) Side (c) Perspective

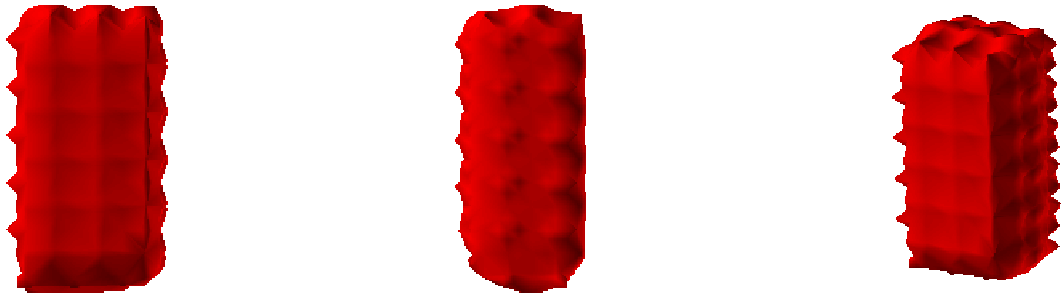

(d) Front, zoomed (e) Side, zoomed (f) Perspective, zoomed

Figure 6: Three views and zooms of the reconstruction of the target number 3 of Table 1 on the once refined mesh. Recall that target number 3 is a ceramic mug.

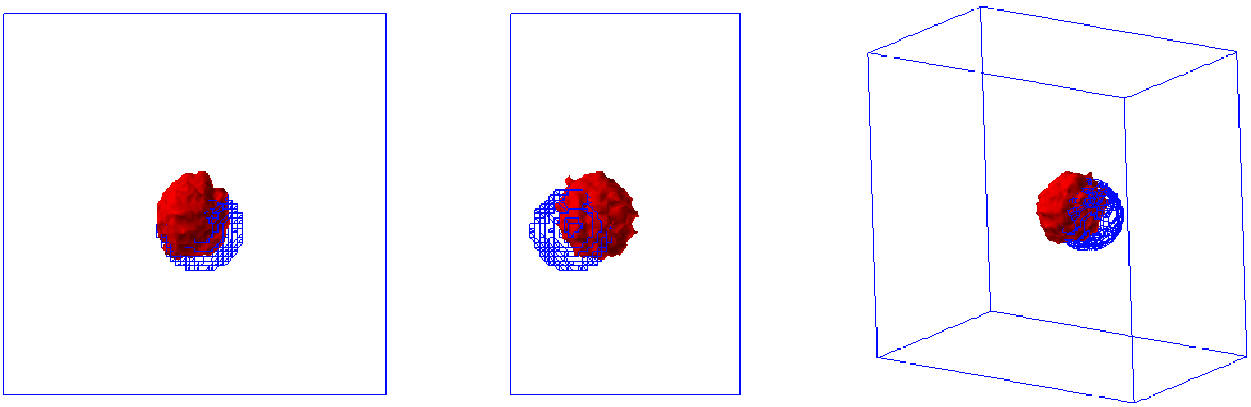

(a) Front (b) Side (c) Perspective

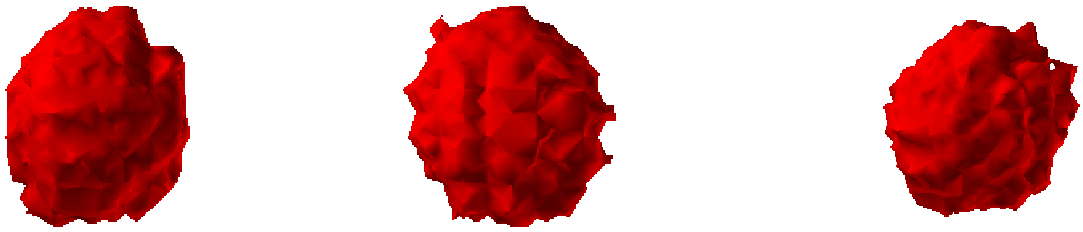

(d) Front, zoomed (e) Side, zoomed (f) Perspective, zoomed

Figure 7: Three views and zooms of the reconstruction of the target number 1 of Table 1 on the three times refined mesh. The initial guess in this test is taken from Test 2 of [22], see Figure 5.1-b),d) of [22]. Recall that target number 1 is a metallic ball.

References

[1] H. Ammari, J. Garnier, J. de Rosny, Knut Solna, Medium induced resolution enhancement broadband imaging, *Inverse problems*, 30, 085006, 2014.

[2] M.Asadzadeh, L.Beilina, A posteriori error analysis in a globally convergent numerical method for a hyperbolic coefficient inverse problem, *Inverse Problems*, 26, 115007, 2010.

[3] M.V. Klibanov, A.B. Bakushinskii and L. Beilina, Why a minimizer of the Tikhonov functional is closer to the exact solution than the first guess? *J. Inverse and Ill-posed problems*, 19, 83-105, 2011

[4] L. Beilina and M.V. Klibanov, Synthesis of global convergence and adaptivity for a hyperbolic coefficient inverse problem in 3D, *J. Inverse and Ill-posed Problems,* 18, 85-132, 2010.

[5] L. Beilina and M.V. Klibanov, *A posteriori* error estimates for the adaptivity technique for the Tikhonov functional and global convergence for a coefficient inverse problem, *Inverse Problems,* 26, 045012, 2010.

[6] L. Beilina, M.V. Klibanov and M.Yu. Kokurin, Adaptivity with relaxation for ill-posed problems and global convergence for a coefficient inverse problem, *Journal of Mathematical Sciences*, 167, 279-325, 2010.

[7] L. Beilina and C. Johnson, A hybrid FEM/FDM method for an inverse scattering problem. In *Numerical Mathematics and Advanced Applications, ENUMATH 2001*, Springer-Verlag, Berlin, 2001.

[8] Beilina, Adaptive hybrid FEM/FDM methods for inverse scattering problems, *Inverse problems and information technologies*, 1 (3), 73-116, 2002

[9] L. Beilina, Energy estimates and numerical verification of the stabilized domain decomposition finite element/finite difference approach for the Maxwell's system in time domain, *Central European Journal of Mathematics*, 11, 702-733, 2013.

[10] L. Beilina, Adaptive Finite Element Method for a coefficient inverse problem for the Maxwell's system, *Applicable Analysis*, 90 (10), 1461-1479, 2011.

[11] L. Beilina and C. Johnson, A posteriori error estimation in computational inverse scattering, *Mathematical Models in Applied Sciences*, 1, 23-35, 2005.

[12] L. Beilina and M.V. Klibanov, *Approximate Global Convergence and Adaptivity for Coefficient Inverse Problems*, Springer, New York, 2012.

[13] L. Beilina, Nguyen Trung Thành, M. V. Klibanov, M. A. Fiddy, Reconstruction from blind experimental data for an inverse problem for a hyperbolic equation, *Inverse Problems* 30, 025002, doi:10.1088/0266-5611/30/2/025002, 2014

[14] L. Beilina, Nguyen Trung Thành, M. V. Klibanov, J.Bondestam Malmberg, Reconstruction of shapes and refractive indices from backscattering experimental data using the adaptivity, to appear in *Inverse Problems*. Preprint, available online at Chalmers Publication Library, http://www.math.chalmers.se/Math/Research/Preprints/, preprint number 2014-9.

[15] S. C. Brenner and L. R. Scott, *The Mathematical theory of finite element methods*, Springer-Verlag, Berlin, 1994.

[16] A.L. Bukhgeim and M.V. Klibanov, Uniqueness in the large of a class of multidimensional inverse problems, *Soviet Math. Doklady*, 17, 244-247, 1981.

[17] F.-C. Chen and W. C. Chew, Experimental verification of superresolution in nonlinear inverse scattering, App. Phys. Lett., 72, issue 23, 3081-3086, 1998.

[18] B. Engquist and A. Majda, Absorbing boundary conditions for the numerical simulation of waves, *Math. Comp.,* 31, 629-651, 1977.

[19] K. Eriksson, D. Estep and C. Johnson, *Calculus in Several Dimensions*, Springer, Berlin, 2004.

[20] A.V. Kuzhuget, L. Beilina, M.V. Klibanov, A. Sullivan, L. Nguyen and M.A. Fiddy, Blind experimental data collected in the field and an approximately globally convergent inverse algorithm, *Inverse Problems*, 28, 095007, 2012.

[21] Nguyen Trung Thành, L. Beilina, M. V. Klibanov and M. A. Fiddy, Reconstruction of the refractive index from experimental backscattering data using a globally convergent inverse method, *SIAM J. Scientific Computing*, 36, B273-B293, 2014.

[22] Nguyen Trung Thành, L. Beilina, M. V. Klibanov and M. A. Fiddy, Imaging of buried objects from experimental backscattering radar measurements using a globally convergent inverse algorithm, Preprint, available online at Chalmers Publication Library, http://www.math.chalmers.se/Math/Research/Preprints/, preprint number 2014-15.

[23] O.Pironneau, *Optimal shape design for elliptic systems*, Springer-Verlag, Berlin, 1984.

[24] F. Simonetti. Localization of pointlike scatterers in solids with subwavelength resolution. *Applied Physics Letter*, 89:094105, 2006.

[25] WavES, the software package, http://www.waves24.com

[26] L. Beilina and M.V. Klibanov, Relaxation property for the adaptivity for ill-posed problems, *Applicable Analysis*, 93(2), 223-253, 2013.